*Burns & Trauma*, 2024, 12, tkae051
https://doi.org/10.1093/burnst/tkae051
Research Article

OXFORD

Research Article

# Suture-anchored cutaneous tension induces persistent hypertrophic scarring in a novel murine model

**Yashu Li[1,†], Anqi Liu[2,3,†], Jingyan Wang[1], Changsheng Yang[1], Kaiyang Lv[1,*], Weifeng He[4,*] and Jun Wu[5,*], and Wenbin Chen[1,*]**

[1]Department of Plastic Surgery, Xinhua Hospital, Shanghai Jiao Tong University School of Medicine, No. 1665 Kangjiang Road, Yangpu District, Shanghai 200092, People's Republic of China, [2]Department of Dermatology, Xiangya Hospital, Central South University, Changsha, Hunan 410008, People's Republic of China, [3]Key Laboratory for the Genetics of Developmental and Neuropsychiatric Disorders (Ministry of Education), Bio-X Institutes, Shanghai Jiao Tong University, Shanghai 200240, People's Republic of China, [4]State Key Laboratory of Trauma, Burn and Combined Injury, Institute of Burn Research, Southwest Hospital, Third Military Medical University (Army Medical University), No. 30 Gaotanyan main Street, Shapingba District, Chongqing 400038, People's Republic of China and [5]Department of Burn and Plastic Surgery, Shenzhen Institute of Translational Medicine, Shenzhen Second People's Hospital, The First Affiliated Hospital of Shenzhen University, No. 3002 Sungang Road, Futian District, Shenzhen 518035, People's Republic of China

*Corresponding author. Kaiyang Lv, E-mail: lvkaiyang@hotmail.com; Wefeng He, E-mail: whe761211@hotmail.com; Jun Wu, E-mail: junwupro@126.com; Wenbin Chen, E-mail: chenwenbin69@163.com

†Yashu Li and Anqi Liu contributed equally to this work.

Received 8 November 2023; Revised 31 December 2023; Editorial decision 29 July 2024

## Abstract

**Background:** Hypertrophic scars cause impaired skin appearance and function, seriously affecting physical and mental health. Due to medical ethics and clinical accessibility, the collection of human scar specimens is frequently restricted, and the establishment of scar experimental animal models for scientific research is urgently needed. The four most commonly used animal models of hypertrophic scars have the following drawbacks: the rabbit ear model takes a long time to construct; the immunodeficient mouse hypertrophic scar model necessitates careful feeding and experimental operations; female Duroc pigs are expensive to purchase and maintain, and their large size makes it difficult to produce a significant number of models; and mouse scar models that rely on tension require special skin stretch devices, which are often damaged and shed, resulting in unstable model establishment. Our group overcame the shortcomings of previous scar animal models and created a new mouse model of hypertrophic scarring induced by suture anchoring at the wound edge.

**Methods:** We utilized suture anchoring of incisional wounds to impose directional tension throughout the healing process, restrain wound contraction, and generate granulation tissue, thus inducing scar formation. Dorsal paired incisions were generated in mice, with wound edges on the upper back sutured to the rib cage and the wound edges on the lower back relaxed as a control. Macroscopic manifestation, microscopic histological analysis, mRNA sequencing, bioinformatics, and *in vitro* cell assays were also conducted to verify the reliability of this method.

**Results:** Compared with those in relaxed controls, the fibrotic changes in stretched wounds were more profound. Histologically, the stretched scars were hypercellular, hypervascular, and

hyperproliferative with disorganized extracellular matrix deposition, and displayed molecular hallmarks of hypertrophic fibrosis. In addition, the stretched scars exhibited transcriptional overlap with mechanically stretched scars, and human hypertrophic and keloid scars. Phosphatidylinositol 3-kinase-serine/threonine-protein kinase B signaling was implicated as a profibrotic mediator of apoptosis resistance under suture-induced tension.

**Conclusions:** This straightforward murine model successfully induces cardinal molecular and histological features of pathological hypertrophic scarring through localized suture tension to inhibit wound contraction. The model enables us to interrogate the mechanisms of tension-induced fibrosis and evaluate anti-scarring therapies.

**Key words:** hypertrophic scar, mouse model, mRNA sequencing, fibrosis, phosphatidylinositol 3-kinase-serine/threonine-protein kinase B

## Highlights

- Few animal models could simply and efficiently replicate key features of human hypertrophic scarring.
- We developed an innovative and reliable murine model which generated scars with histological and molecular features resembling human pathological fibrosis by utilizing suture anchoring to restrain wound contraction throughout the healing process without repeated animal restraint or mechanical equipment that could cause general confounders.
- This model enables unraveling of the mechanisms of tension-induced fibrosis and the development of targeted anti-scarring therapies.

## Background

Hypertrophic scars typically arise in skin areas with high tension, including the shoulders, presternal area, lower abdomen, and chin. Reducing mechanical tension is currently regarded as an effective preventive method for hypertrophic scar formation [1–4]. Increased mechanical stress in the wound environment induces hypertrophic scarring by activating key mechanotransduction network components such as transforming growth factor-$\beta$ (TGF-$\beta$), focal adhesion kinase (FAK), myocardin-related transcription factor-A (MRTF-A), Yes-associated protein (YAP), Engrailed-1, and Wnt-$\beta$-catenin. Mechanical forces dramatically trigger the release, activation, and bioavailability of TGF-$\beta$1 [5]. Fibroblast contraction and TGF-$\beta$1 activation create a feedback loop on a stiff matrix that amplifies matrix deposition and fibrotic pathologies [6]. FAK contributes to fibroblast activation and promotes the expression of TGF-$\beta$1, alpha-smooth muscle actin ($\alpha$-SMA), collagen I, and fibronectin in hypertrophic scars [4]. Furthermore, FAK causes a chronic-like inflammatory state via extracellular-related kinase (ERK) to physically stimulate the release of monocyte chemoattractant protein-1 (MCP-1) [7, 8]. MRTF-A is required for matrix stiffness-induced $\alpha$-SMA expression and myofibroblast differentiation [9]. Through engagement of TEA domain transcription factor 1 and subsequent de novo expression of MRTF-A, YAP collaborates with TGF-$\beta$1 to promote myofibroblast differentiation and matrix stiffening [10–12]. Engrailed-1 is activated by mechanical tension via YAP signaling. Preventing Engrailed-1 activation enhances wound regeneration by restoring skin appendages, ultrastructure, and mechanical strength [13]. Wnt-$\beta$-catenin cooperates with TGF-$\beta$ to facilitate adipocyte lipolysis and adipocyte-to-myofibroblast transition during wound healing, which promotes fibrogenic development in keloids [14]. However, the molecular events linking tension to cutaneous fibrosis have not been fully defined.

Establishing scar experimental animal models for scientific research is urgently needed, as human skin scar tissues are difficult to collect due to ethical and practical considerations. However, the current animal models of hypertrophic scars have the following disadvantages. The development of a rabbit ear model requires a lengthy period of time [15], while the hypertrophic scar model in immunodeficient mice necessitates rigorous feeding and experimental operation [16]. Due to their great size and high cost of purchase and upbringing, female Duroc pigs have difficulty producing a significant number of models [17]. The mouse dorsal wound model is simple to manipulate and commonly utilized in research [18]. However, the strong elasticity of murine skin, loose space between the skin and subcutaneous tissue, and tendency to contract in subcutaneous panniculus carnosus all cause drastic wound shrinkage during healing. In addition to re-epithelialization, human wounds heal primarily through the development of granulation tissue rather than through wound contraction [19]. Inhibiting wound shrinkage and simulating the process of human granulation tissue formation on mouse skin may be helpful for modeling murine scars. Several advances in mouse models have been made to conquer wound contraction by utilizing external silicone splints [20]. However, mice are active and silicone splints are easily destroyed during experiments, resulting in poor modeling stability. Mechanical devices applied on healed wounds were

verified to induce hypertrophic scarring resembling human hypertrophic scarring [21]. However, this method does not mimic granulation tissue formation during wound healing and thus does not precisely simulate scarring processes in humans, where local stress persists at the onset of healing. Moreover, these materials are unstable because mechanical devices are prone to loosening and dropping.

Here, we present a novel murine model of hypertrophic scarring that overcomes the shortcomings of previous scar animal models. Specifically, dorsal skin is stretched from the midline incision to both sides, the wound edge is anchored on the ribs at the midaxillary line with sutures, wound contraction is conquered, and chronic granulation is gradually formed, thus inducing hypertrophic scar formation, which simulates the formation of human scars. Morphologic and histology analyses confirmed the development of fibroproliferative scars in this model. mRNA sequencing and bioinformatics analysis revealed gene expression patterns consistent with those of the current hypertrophic scar model and human keloid scars. *In vitro*-cultured fibroblasts implicated phosphatidylinositol 3-kinase (PI3K)-serine/threonine-protein kinase B (Akt) signaling as a mediator of apoptotic resistance and tension-induced fibrosis. Overall, this innovative murine model is a simple, reliable, and economic model for investigating the mechanisms and therapeutic strategies used to treat hypertrophic scars.

## Methods

### Mice and modeling procedures

C57BL/6 wild-type mice aged 6-8 weeks were used for modeling. All procedures were carried out with the approval of the Animal Ethics Committee of Xinhua Hospital. Hair on the dorsal skin was removed by an electrical hair cutter and depilatory cream. After the limbs were lengthened and fasted, '▲', '△' and '▽' were labeled on the posterior midline, the midaxillary line, and the line between '▲' and '△', respectively. The upper dorsal skin on line '▽' was then sutured to the ribs and intercostal muscles under line '△' with 6-0 nylon thread. The lower back skin on line '▽' was sutured *in situ* to the subcutaneous tissue. Finally, 1 cm linear wounds were cut between the fixed skin along lines '▲'. A liner incision on the upper dorsal skin was designated the stretched group, while wounds on the lower dorsal skin were considered the control group.

### Morphometry by the Vancouver scar scale

The scars were photographed at weeks 2, 12, and 24 after injury. Then, the scars and adjacent skin were harvested from the stretched and control groups, respectively. The scars were graded on melanin, height, vascularity, and pliability according to the Vancouver scar scale (VSS) [22]. The total score was 15, with a higher score indicating more extensive scar hyperplasia.

### Histologic analysis

Tissue specimens were fixed with paraformaldehyde, embedded in paraffin and sectioned along the median axis. Sections 5 $\mu$m in thickness were stained with hematoxylin and eosin (H&E) (Servicebio, China) to evaluate the total scar area [21]. The visibility of collagen fibers was improved, as shown by Masson's trichrome staining (Servicebio, China) [23]. The architecture of the stretched and control scars was examined by an Olympus BX51 microscope (Tokyo, Japan). Picrosirius red staining (Servicebio, China) was used to assess the type of collagen fibers, which were photographed by a polarized light microscope (Nikon Eclipse Ci-L, Japan) [24]. The sections were analyzed by Image-Pro Plus 6.0 (Media Cybernetics, USA). The presence of scars was confirmed by horizontally oriented collagen bundles and the absence of skin appendages. The width of the scars was determined as the distance between intact hair follicles. The scar elevation index (SEI) is a reliable and repeatable tool for assessing the establishment of hypertrophic scars. The SEI is the ratio of the entire scar dermal area, including the newly produced hypertrophied dermis, to the area of the normal dermis of the surrounding unwounded skin, and was calculated as follows: SEI = $H_{\text{scar dermis}}/H_{\text{normal dermis}}$. As measured from the bottom point of the epithelium to the surface of the subcutaneous fat layer in the scar tissue and adjacent normal tissue, the $H_{\text{scar dermis}}$ represents the maximum thickness of the scar dermis, and the $H_{\text{normal dermis}}$ represents the maximum thickness of the normal dermis around the scar tissue [23]. The images were evaluated blindly by two independent observers and the results were not significantly different. The data are presented as the means ± SDs.

### Immunohistochemical staining

The expression levels of the indicated targets in scars were detected by immunohistochemical staining as previously described [25]. Scar sections were deparaffinized and hydrated in xylene and a graded alcohol series. Antigen retrieval was accomplished by heating the slices in 10 mM citric acid (pH 6) (Servicebio, China) for 15 min at 95°C. Sections were blocked with goat-anti-rabbit serum or 3% bovine serum albumin with 0.3% Triton X-100 (Sigma-Aldrich, Germany) for 1 h at room temperature. Then, the sections were incubated with antibodies against $\alpha$-SMA (1 : 200), CD31 (1 : 300), Ki67 (1 : 500), and TGF-$\beta$ (1 : 200) (Servicebio, China) at 4°C overnight. Next, the slices were thoroughly washed with phosphate buffered saline (PBS) (Servicebio, China) and incubated with secondary antibodies for 30 min at room temperature. This was followed by incubation with drops of diaminobenzidine solution (Boster, China) and counterstaining with hematoxylin (Beyotime, China). The stained sections were assessed using an Olympus BX51 microscope (Tokyo, Japan). The investigators were blinded during histologic staining. Representative images were selected for the figures.

### Immunofluorescence staining

Fresh scar tissue was obtained for frozen sectioning. A terminal deoxynucleotidyl transferase dUTP nick-end labeling (TUNEL) assay (Servicebio, China) was also conducted according to the manufacturer's instructions. Proteinase K was used to prepare frozen tissue sections. The TUNEL reaction mixture was incubated after the sample was permeabilized. The sections were nucleated with 4',6-diamidino-2-phenylindole (Servicebio, China), sealed with an anti-fluorescein quencher, and then photographed by fluorescence microscopy (K10587, Nikon, Tokyo, Japan).

### Quantitative real-time PCR

Quantitative real-time PCR (qRT-PCR) was conducted as previously reported [25]. Briefly, RNA was extracted using TRIzol reagent (Thermo Scientific, USA). A TaqMan reverse transcription kit was used to produce cDNA according to the manufacturer's instructions (Life Technologies, USA). With a Bio-Rad RT-PCR system, qRT-PCR was performed with SYBR Green Supermix. The primers used in this study were generated by Sangon Biotech (Shanghai, China). The expression levels of mRNA were standardized to those of GAPDH, and the fold differences were determined by the following method: $F = 2^{-\Delta\Delta Ct}$, $\Delta Ct = Ct_{\text{target gene}} - Ct_{GAPDH}$ and $\Delta\Delta Ct = \Delta Ct_{\text{induced}} - \Delta Ct_{\text{reference}}$.

### Cell culture

The method for culturing cells under different tensions was described by Achterberg *et al*., who used silicone substrates to simulate a soft skin matrix and plastic substrates as a stiff matrix [26]. Silicone substrates (CytoSoft®) were purchased from Sigma-Aldrich (St Louis, MO, USA) and were prepared with varying stiffnesses to mimic the elastic range of normal (2 kPa) and fibrotic (64 kPa) dermis. Substrate surfaces were coated with 0.2 $\mu$g/cm$^2$ rat tail collagen type I (Yeason, Shanghai, China). Human foreskin fibroblast (HFF-1) cells were obtained from Zhong Qiao Xin Zhou Biotechnology Co., Ltd (Shanghai, China). HFF-1 cells were grown in Dulbecco's Modified Eagle Mediumsupplemented with 15% fetal calf serum for 48 h. MK-2206 (MCE, USA) is a selective inhibitor for Akt phosphorylation. MK-2206 (5 $\mu$mol/l) was added to cultured HFF-1 cells and dimethyl sulfoxide was used as a control. In selected experiments, 5 ng/ml TGF-$\beta$1 (Sigma-Aldrich) was added to stimulate HFF-1 cells. The HFF-1 cells were analyzed for collagen I and fibronectin levels by qRT-PCR; Akt (1 : 1000), phosphorylated Akt (1 : 1000), caspase-3 (1 : 1000), cleaved caspase-3 (1 : 1000) (CST, USA), and TGF-$\beta$1 (1 : 1000 (Abcam, UK) levels were determined via western blotting; and Annexin V-IF647/Propidium Iodide (PI) cell apoptosis (Servicebio, China) was detected via flow cytometry.

### Western blot

The scar and surrounding 1–2 mm wide tissue were collected. Total protein was extracted from the tissues as described previously. A bicinchoninic acid assay protein assay kit (Thermo Scientific, Rockford, USA) was used to determine the concentration of the extracted protein. The protein concentration was adjusted to 25 $\mu$g/well by 10 or 12% sodium dodecyl sulfate-polyacrylamide gel electrophoresis. The samples were subsequently transferred to polyvinylidenedifluoride (PVDF) membranes (Millipore Immobilon, USA). The PVDF membranes were treated for 2 h at room temperature with 3% bull serum albumin (Biosharp, China) and then incubated overnight at 4°C with anti-TGF-$\beta$1 (1 : 1000, Abcam, UK), anti-Akt (1 : 1000), anti-phospho-Akt (Thr308) (1 : 1000), anti-caspase-3 (1 : 1000), and anti-cleaved caspase-3 (1 : 1000) (CST, USA) antibodies. The PVDF membranes were incubated for 1 h at room temperature with goat-anti-rabbit/mouse/rat-horseradish peroxidase immunoglobulin G (1 : 5000; SunGene Biotech, China), and for seconds with chemiluminescence solution (Solarbio, China). A ChemiDocTM XRS detection system (Bio-Rad, USA) was used to measure the protein concentration as described previously [25].

### Flow cytometry

An Annexin V-IF647/PI cell apoptosis detection kit was purchased from Servicebio Technology Co., Ltd (Wuhan, China). First, the supernatant from the cell culture was collected. Following EDTA-free pancreatic enzyme digestion, the cells were put together with culture supernatant. Then, the cells were collected after centrifugation at 500 g and 4°C for 5 min. Before being centrifuged twice at 500 g for 5 min each, the cells were washed twice with precooled PBS. They were then gently suspended in precooled 1× binding buffer to adjust the cell concentration to 1–5 × 10$^6$/ml. Then 100 $\mu$l of cell suspension was taken, 5 $\mu$l of Annexin V-IF647 and 5 $\mu$l of PI was added and gently mixed, while avoiding light, at room temperature for 8–10 min. As previously reported [25], the stained cells were detected by Attune Acoustic Focusing Cytometer (Life Technologies, USA) and analyzed with FlowJo software (Tree Star Incorporation, USA).

### mRNA sequencing and bioinformatics

High-throughput RNA sequencing was performed by Cloud-Seq Biotech (Shanghai, China). Briefly, total RNA was extracted from samples ($n = 3$ per group) of stretched induced hypertrophic scars (HS) and control normal scars (NS) 2 weeks after excision. The RNA was subsequently subjected to analysis with a GenSeq® rRNA removal kit (GenSeq, Inc.) to remove the rRNAs, and the rRNA-depleted samples were utilized for library construction with a GenSeq® low-input RNA library prep kit (GenSeq, Inc.). Libraries were quantified and quality controlled by a BioAnalyzer 2100 system (Agilent Technologies, Inc., USA). Library sequencing was conducted on an Illumina NovaSeq instrument with 150 bp paired-end reads. Paired-end reads were obtained from an Illumina NovaSeq 6000 sequencer and were quality controlled using Q30. The 3′ adaptor and low-quality reads were removed by Cutadapt software (v1.9.3). Next,

the high-quality clean reads were aligned to the reference genome (build GRCm38) with HISAT2 software (v2.0.4). The raw count was harvested from HTSeq software (v0.9.1) and normalization was performed via edgeR. The raw RNA sequencing data were uploaded to Gene Expression Omnibus (GEO) (GSE243950). Differentially expressed genes (DEGs) were identified by *P*-value, false discovery rate (FDR), and fold-change (log2) across all group comparisons. Uniform manifold approximation and projection (UMAP) was conducted to evaluate the grouping of samples [27]. Genes were ranked according to their absolute expression or fold-change in HS and NS. Heatmap and hierarchical cluster analysis, scatter plots, and volcano plots of RNA-sequencing data from HS and NS samples were generated by Cloudseq.

### Functional enrichment analysis

DEGs were compared at the statistical significance level of FDR < 0.05. Up- and down-regulated DEGs were subjected to functional enrichment analysis using the Gene Ontology (GO) biological process, cellular components, and molecular function [24]. In addition, the upregulated DEGs were enriched according to the cluster circle diagram and chord diagram generated by Kyoto Encyclopedia of Genes and Genomes (KEGG) analysis [28]. The R studio packages 'clusterProfiler', 'org.Mm.eg.db', 'ggplot2', 'enrichplot', and 'GOplot' were used for data visualization. Venn diagrams (http://bioinfogp.cnb.csic.es/tools/venny/index.html) illustrate the proportions of entities within the up- or down-regulated DEGs that were found in the core matrisome and matrisome-associated gene sets [29]. The DEGs found in subcategories of core matrisome and matrisome-associated datasets were visualized via heatmaps and non-average hierarchical clustered intensity plots. The published transcriptome data for stressed scars (SS) and unstressed scars (US) initiated by mechanical loading devices [8] were obtained from the GEO (GSE26390). A Venny diagram was constructed to plot the shared up- or down-regulated DEGs between the HS and NS groups and between the SS and US groups. Functional enrichment of the shared genes was conducted using the GO and Reactome databases (https://reactome.org/PathwayBrowser/#TOOL=AT). The top ten Reactome terms are organized in a table. The interactions between target DEGs were analyzed by the Search Tool for the Retrieval of Interacting Genes (STRING) database (https://string-db.org/) to construct a protein–protein interaction network. Cell type enrichment was performed via the ImmGen MyGeneSet web tool [30].

### Gene-set enrichment analysis

Significantly up- and down-regulated gene sets were derived from the GEO for published transcriptomic data and published RNA-seq data on extracellular matrix (ECM) remodeling genes, fibroblast related genes, wound-derived myofibroblast subsets, keloid fibroblasts, and keloid keratinocytes. The original gene sets were uploaded to gene-set enrichment analysis (GSEA) version 4.2.3 [31], filtered to those mapped by gene symbol and presented in the tested datasets. The gene sets were tested against the transcriptomes of HS vs. NS. The GSEA results are displayed as enrichment plots and arranged in tables where the normalized enrichment scores (NES), nominal *P* value (NOM p-val) and FDR values are color coded for visualization [24]. The GSEA-specific source data file for Figure 6 contains the previously published datasets and samples examined, original and filtered gene sets, GSEA parameters used for each analysis, ranked gene lists, and original GSEA output data for all studies.

### Statistical analysis

Statistical analysis was performed using GraphPad Prism 8 software for Windows (San Diego, CA, USA). Two groups were analyzed by the two-sided Student's paired t test. One-way analysis of variance (ANOVA) and Bonferroni's multiple comparisons *post hoc* tests were used for comparisons of more than two groups. Two-way ANOVA and Sidak's multiple comparative tests were used for the comparison of two collagen types between two groups. The F test, Brow–Forsythe test and Levene's test were performed to verify equal variance via Student's paired t test, one-way ANOVA, and two-way ANOVA, respectively. The purpose of the variance homogeneity test is to determine the appropriate statistical methods. In this investigation, uneven variance was not detected. *P* values of the statistical comparisons are displayed in the figures ($^{*}p < 0.05$, $^{**}p < 0.01$, $^{***}p < 0.001$).

## Results

### Suture-anchored tension induced pathological scarring in murine excisional wounds

To impose tension during cutaneous wound healing, we developed a novel mouse model using suture-anchored incisions. Dorsal excisional wounds were generated via transverse-axial stretching by anchoring the upper wound edges to the rib cage while leaving the lower edges unattached (Figure 1a, Figure S1, see online supplementary material). At 2 weeks after the operation, stretched scars displayed significantly greater VSS scores for pigmentation, vascularity, height, and pliability 2 weeks post-wounding (Figure 1b, Table 1). Scars were adherent to the underlying tissue in the stretched group only 2 weeks after excision (Figure 1c). Histological analyses revealed pathological matrix remodeling under tension. Stretched scars showed increased width, epidermal hyperplasia without rete ridges, absent adnexal structures, disorganized dermal collagen, and an increased SEI (Figure 1d–f). Masson's trichrome staining revealed that, compared with that in the controls, the collagen in the stretched scars was hyperplastic (Figure 1g). The amount of red blood cells filling in the stretched scars was significantly higher than in controls (Figure 1h), which was consistent with the fact that stretched

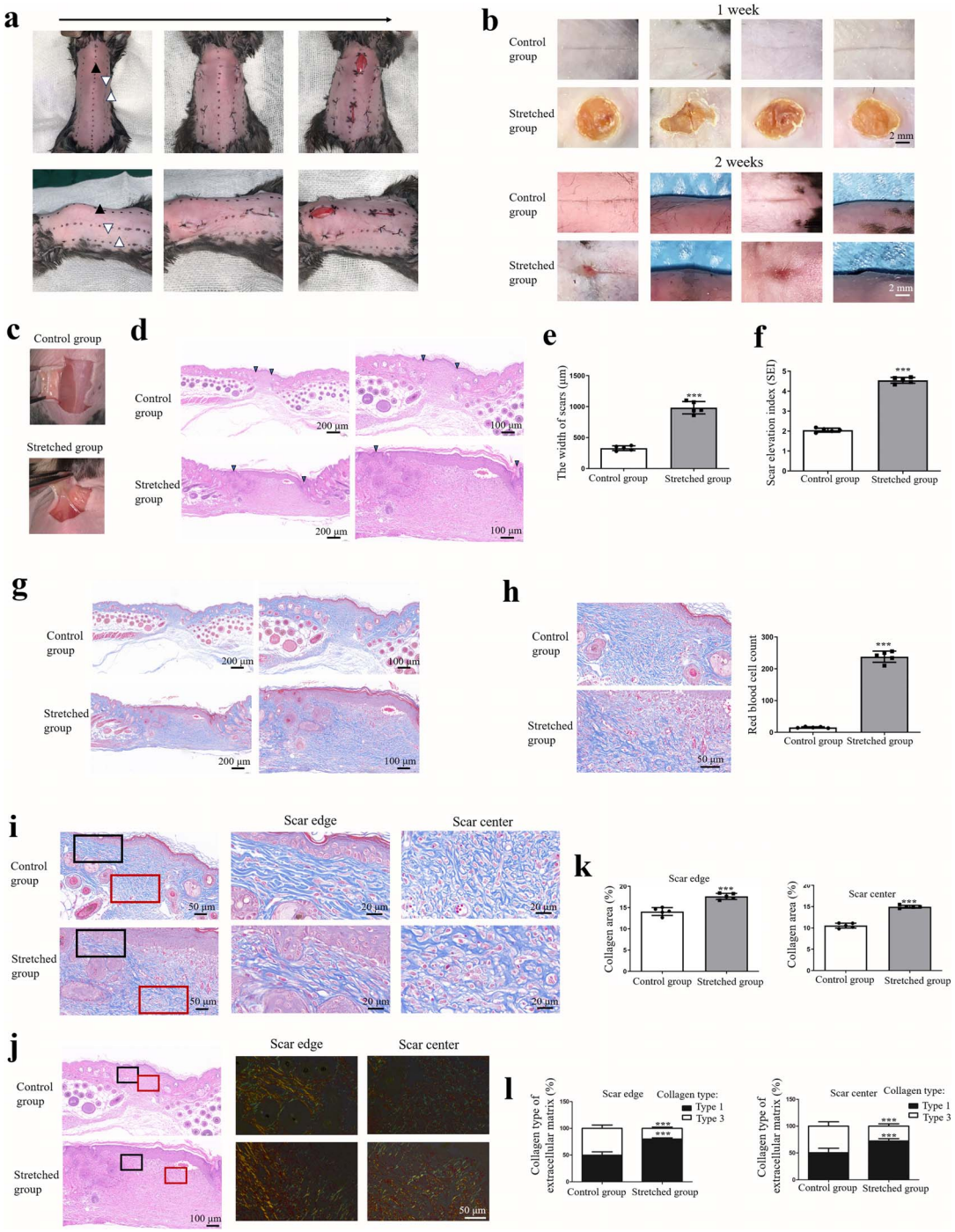


**Figure 1.** Suture-induced local stress resulted in hypertrophic scars 2 weeks after surgery. (**a**) Suturing the dorsal skin caused local tension in this model. The posterior median line and the midaxillary line were labeled '▲' and '△', respectively; the line between '▲' and '△' was labeled '▽'. Then the upper dorsal skin on '▽' was sutured to the ribs and intercostal muscles beneath '△' and served as the experimental group, whereas the lower dorsal skin of '▽' was fixed *in situ* to subcutaneous tissue and functioned as the control. Finally liner incisions with 1 cm width were cut along '▲' between the fixed upper and lower dorsal skin. (**b**) Representative macroscopic photographs of local stress-induced scars and non-stretched controls at weeks 1 and 2 post-operation. Stretch scars and controls were evaluated at week 2 post-excision. Scars were assessed by the VSS ((Scale bar: 2 mm). (**c**) Subcutaneous tissue adhesion in stretched scars and controls. (**d**) H&E staining of stretched scars and controls. Scar edges are indicated by inverted triangles (Scale bar: 200 $\mu$m & 100 $\mu$m). (**e**) Scar width in stretched groups and controls. (**f**) Difference in SEI between stretched scars and controls. (g–i) Stretched scars and controls were examined by Masson's trichrome staining. (**g**) Representative Masson's trichrome staining (Scale bar: 200 $\mu$m & 100 $\mu$m). (**h**) High magnification of the scar center and quantification of red blood cells (Scale bar: 50 $\mu$m). (**i**) Comparison of scar centers and edges in stretched and control groups (black rectangles: scar edges; red rectangles: scar centers, Scale bar: 50 $\mu$m & 20 $\mu$m). (j–l) Stretched scars and controls were analyzed by picrosirius red staining. (**j**) Picrosirius red staining of stretched scars and controls (black rectangles: scar edges; red rectangles: scar centers, Scale bar: 100 $\mu$m & 50 $\mu$m). (**k**) Percentage of collagen in ECM was calculated in the centers and edges of stretched scars and controls. (**l**) Proportions of collagen type 1 and 3 in scar edges and centers. Two-tailed Student's t-test (e, f, h, k). Two-way ANOVA and Sidak's multiple comparative tests (l). $^{***}p < 0.001$. *H&E* hematoxylin and eosin, *SEI* scar elevation index, *ECM* extracellular matrix, *ANOVA* analysis of variance

**Table 1.** Local stretching caused scars with higher Vancouver scar scale scores in comparison to controls 2 weeks post-operation.

| Groups | Samples | Melanin | Vascularity | Height | Pliability |
|---|---|---|---|---|---|
| Control | 10 | 0 | 0 | 0 | 0 |
| Stretched group | 10 | $2.30 \pm 0.46$ | $1.80 \pm 0.40$ | $2.20 \pm 0.40$ | $4.5 \pm 0.81$ |
| *P* value | | <0.0001 | <0.0001 | <0.0001 | <0.0001 |

scars appeared redder than did the controls (Figure 1b). Collagen fibers appeared irregularly arranged at the wound edges and lacked clear borders or orientation in the scar center (Figure 1g). Collagen types 1 and 3 constitute the majority of adult skin collagen, accounting for 80–85% and 10–15% respectively, of skin weight [32]. Type 1 collagen, which is dense, provides skin tensile strength, whereas type 3 collagen is fine. The composition and proportion of collage fibers in scars are different from those in normal skin. Upregulated type 1 collagen leads to scar fibrosis [33]. Picrosirius red staining demonstrated increased collagen content in stretched scars (Figure 1j, k), predominantly type I collagen (Figure 1l). These features resembled those of human hypertrophic scars.

At 12 weeks after surgery, stretching-induced scars were still visible (Figure 2a). The scar width and SEI were greater in the stretched group than in the control group (Figure 2b–d). The collage in stretched scars remained hyperplastic (Figure 2e) and was still filled with more red blood cells than that in controls (Figure 2f). Central collagen fibers began swirling into nodules, a characteristic manifestation of chronic fibroproliferation (Figure 2g). Picrosirius red staining demonstrated that the collagen content remained increased in the stretched scars 12 weeks after surgery (Figure 2h, i). According to the histological criteria, the scars had stabilized for 24 weeks but hyperplasia had subsided further (Figure 2a–d). These results indicated that over 24 weeks, the stretched scars progressed through the hyperplastic, regressive, and maturation phases. The suture-anchored tension model thus successfully induced sustained pathological matrix remodeling analogous to human fibroproliferative scarring.

To evaluate the technical reliability, we performed the tension model across five cohorts, each with 10 mice. The success rate in inducing fibroproliferative scars was $90 \pm 7.07\%$. This finding confirms that the suture-anchored method is a robust, facile approach for modeling cutaneous scarring. Several advantages of this murine model for investigating the mechanisms of tension-induced fibrosis are recommended. The two wounds on upper and lower back were generated on each mouse control for individual differences. Local suture anchoring imposes persistent, directional tension throughout healing without repeated animal restraint or mechanical equipment. The dorsal wounds are easily accessed for macroscopic and histological assessment at serial time points.

## Stretched scars displayed molecular hallmarks of hypertrophic fibrosis

To further characterize the pathological scarring induced by suture-anchored tension, we examined the expression of proteins involved in fibroproliferation and inflammation. Myofibroblasts expressing $\alpha$-SMA are responsible for aberrant collagen deposition during fibrotic healing, which is a hallmark of human hypertrophic scarring [34]. At 2 weeks post-operation, compared with those of the relaxed controls, the stretched scars had dramatically more $\alpha$-SMA-positive cells (Figure 3a). Angiogenesis supplies the hypercellularity of fibroproliferative scars [35]. Figure 1h shows that more red blood cells filled the stretched scars than those in the controls. Moreover, immunostaining for the endothelial marker CD31 revealed a significantly greater microvessel density in stretched scars at week 2 (Figure 3b), indicating that suture-anchoring stress induced hypervascularity in this model. Cell proliferation was increased in stretched scars, as indicated by the presence of expanded Ki67-positive epidermal and dermal cells (Figure 3c). Concurrently, the epidermis was thicker in the stretched wounds. Several profibrotic factors showed heightened expression in stretched scars at week 2. TGF-$\beta$, a well-known promoter of fibrosis [8], was upregulated in the dermis of stretched scars (Figure 3d). By 12 weeks post-wounding, the stretched scars retained increased levels of $\alpha$-SMA, CD31, and Ki67 compared to those in the controls, while TGF-$\beta$ expression had normalized (Figure S2, see online supplementary material). At the 24-week, $\alpha$-SMA and CD31 remained upregulated in the stretched group (Figure S3, see online supplementary material).

To summarize, suture-anchored tension induces vital molecular characteristics of hypertrophic scarring, including myofibroblast persistence, neovascularization, proliferation, and profibrotic signaling. The changes in the expression of $\alpha$-SMA, CD31, Ki67 and TGF-$\beta$ during scar remodeling further suggested that this model could resemble human hypertrophic scarring.

## Transcriptomic profiling revealed a fibrogenic signature in tension-induced hypertrophic scars

To elucidate the molecular mechanisms underlying the pathological matrix remodeling induced by suture-anchored tension, we performed mRNA sequencing on 2-week scar samples. Unsupervised UMAP clustered stretched HS

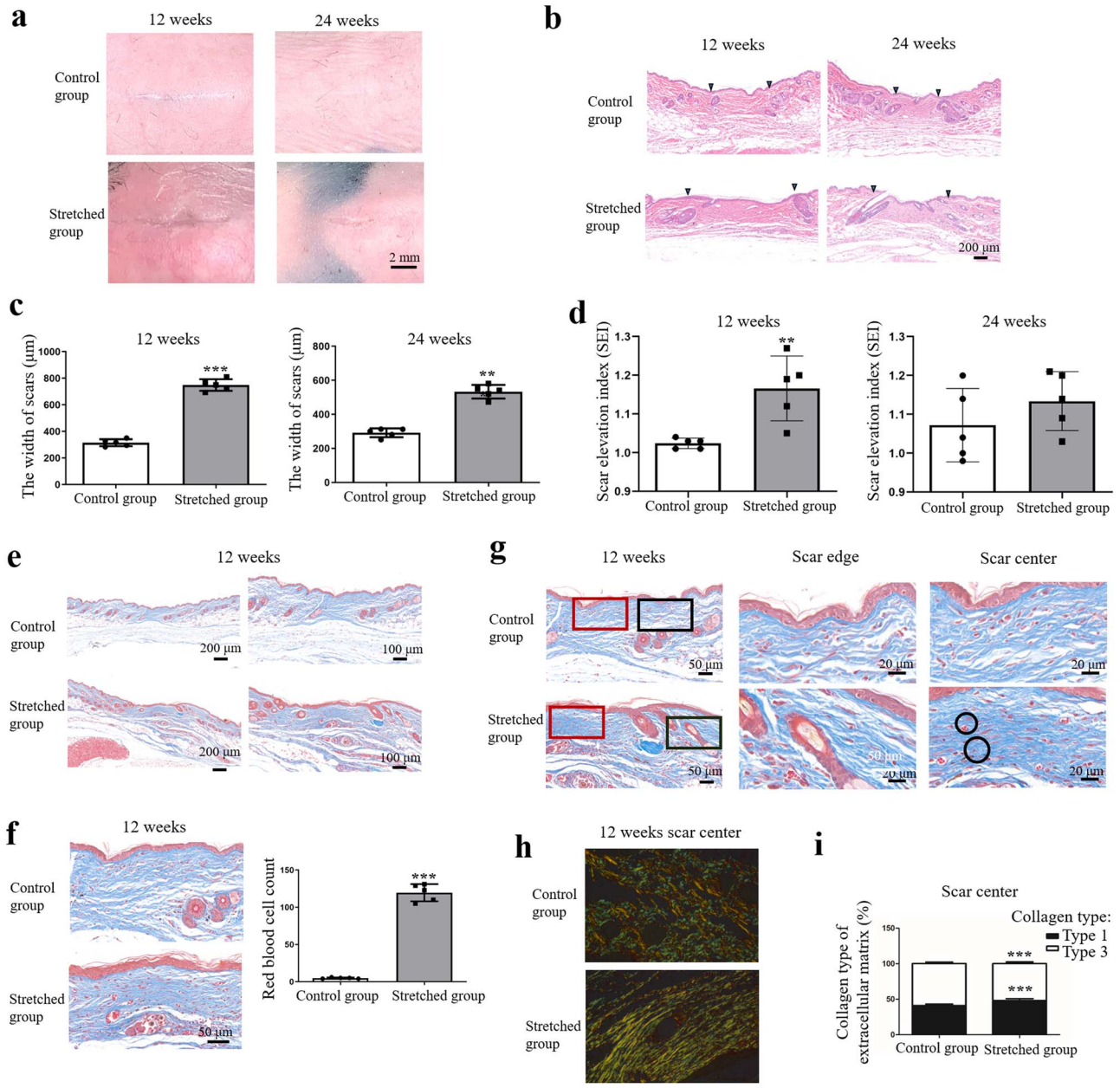


**Figure 2.** Stretching-induced hyperplasia was sustained long-term up to 3 months post-wounding. (**a**–**d**) Scars were assessed in stretched and control groups at weeks 12 and 24 post-operation. (**a**) Representative macroscopic images of stretched and control scars (Scale bar: 2 mm). (**b**) H&E staining of stretched scars and controls. Scar edges are indicated by inverted triangles (Scale bar: 200 $\mu$m). (**c**) Width of scars. (**d**) SEI. (**e**–**g**) Stretched scars and controls were examined by Masson's trichrome staining 12 weeks after excision. (**e**) Representative Masson's trichrome staining (Scale bar: 200 $\mu$m & 100 $\mu$m). (**f**) High magnification of the scar center and quantification of red blood cells (Scale bar: 50 $\mu$m). (**g**) Comparison of scar centers and edges in stretched and control groups (black rectangles: scar edges; red rectangles: scar centers, Scale bar: 50 $\mu$m & 20 $\mu$m)). (**h**, **i**) Stretched scars and controls were analyzed by picrosirius red staining at week 12 post-excision. (**h**) Representative picrosirius red staining of scar centers in stretched and control groups. (**i**) Percentages of collagen type 1 and 3 in centers of stretched scars and controls. Two-tailed Student's t-test (**c**, **d**, **f**). Two-way ANOVA and Sidak's multiple comparative tests (**i**). $^{**}p < 0.01$, $^{***}p < 0.001$. *H&E* hematoxylin and eosin, *SEI* scar elevation index, *ANOVA* analysis of variance

separately from relaxed NS, indicating distinct transcriptional profiles (Figure 4a). Differential expression analysis identified a total of 1011 genes upregulated and 168 genes downregulated in the HS group compared with the NS group ($p < 0.05$) (Figure 4b–e). With an FDR < 0.05, 525 upregulated and 60 downregulated DEGs were identified in the HS (Figure 4e). The top 10 most highly expressed genes in HS were collagen genes *Col3a1* and *Col1a2*, along with ECM proteins *Sparc*, *Lum*, *Mmp2*, and *Fn1*, which were all upregulated compared to NS (Figure 4f).

GO analysis revealed that the upregulated HS genes were enriched in ECM organization, collagen metabolism, angiogenesis, inflammation, and cytokine production (Figure 5a, Figure S4a, see online supplementary material). KEGG

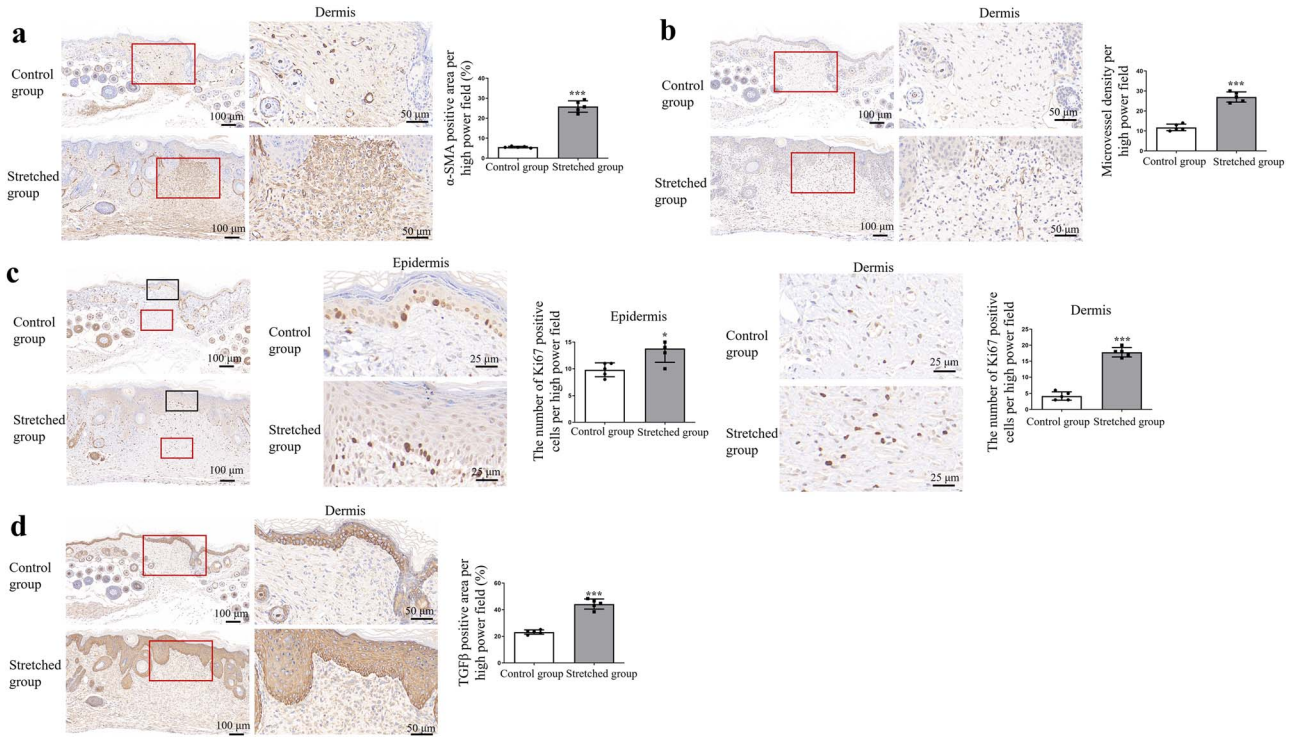


**Figure 3.** Stretched scars expressed hypertrophic scar markers. (**a–d**) Stretched and control scars were stained with the following markers 2 weeks after surgery. Red rectangles mark the dermis of scar center. (**a**) Representative $\alpha$-SMA staining graphs, and the proportions of $\alpha$-SMA-positive area in the centers of control and stretched scars (Scale bar: 100 $\mu$m & 50 $\mu$m). (**b**) CD31 staining sections and microvessel density in the centers of stretched scars and controls (Scale bar: 100 $\mu$m & 50 $\mu$m). (**c**) Ki67 staining graphs with black rectangle representing the epidermis of scar center. The number of Ki67 positive cells was calculated respectively in the epidermis and dermis of stretched and control scars (Scale bar: 500 $\mu$m & 25 $\mu$m). (**d**) Graphs with TGF-$\beta$ staining, and TGF-$\beta$ positive percentages in control and stretched groups (Scale bar: 100 $\mu$m & 50 $\mu$m). Values were analyzed by two-tailed Student's t-test. $^{*}p < 0.05$, $^{***}p < 0.001$. *TGF-$\beta$* transforming growth factor-$\beta$, *$\alpha$-SMA* alpha-smooth muscle actin

pathway analysis showed enrichment of genes related to ECM–receptor interactions, PI3K-Akt signaling, proteoglycan metabolism, and focal adhesions (Figure 5b, Figure S4b, see online supplementary material). FAK and PI3K-Akt signaling mediate mechanotransduction and prevent fibroblast apoptosis during fibrosis [8, 21]. The downregulated DEGs in HS *vs* NS were associated with fiber components, actin binding and embryonic patterning, 8 Homeotic (HOX) genes whose expression was downregulated indicated a 'tumorigenic phenotype' of keloids [36] (Figure S5, see online supplementary material).

To specifically interrogate matrix remodeling pathways, we analyzed the matrisome signature. The matrisome comprises core ECM proteins plus matrisome-associated interacting and regulatory factors. Among the 274 core matrisome genes, 52 were upregulated and only 1 was downregulated in the HS group (Figure 5c,d). Collagens represented the majority of altered core matrisome components. A total of 34.9% of the collagen genes were upregulated without any downregulation (Figure 5c). The fibrillar collagens *Col3a1*, *Col1a2*, and *Col1a1* showed the highest expression (Figure 5e), consistent with increased collagen I deposition under tension (Figure 1l). Stretching also increased the expression of collagens V (*Col5a2*, *Col5a1*), VI (*Col6a1*, *Col6a2*, *Col6a3*, *Col6a5*, *Col6a6*), VII (*Col7a1*), VIII (*Col8a1*), XII (*Col12a1*), XIV (*Col14a1*), and XXVII (*Col27a1*), which are involved in regulating collagen fibrillogenesis and interactions. Proteoglycans help maintain ECM integrity [37]. HS exhibited upregulation of the proteoglycans *biglycan*, *lumican*, *asporin*, *podocan*, and *hyaluronan link protein 4* (Figure 5e). Glycoproteins, the largest matrisome family, presented 29 upregulated genes and 1 downregulated gene in the HS group. The top-upregulated glycoproteins were *tenascin*, *osteopontin* (*Spp1*), *tenascin C* (*Tnc*), and *Cthrc1* (Figure 5e). Beyond the core matrisome components, the matrisome-associated cluster contained 836 matrix-affiliated genes. HS exhibited 75 upregulated and only 4 downregulated matrisome-associated genes (Figure 5c,d). The most highly upregulated 'extracellular matrisome affiliates' included regenerating islet-derived 1 (*Reg1*), C-type lectin domain family 2 member e (*Clec2e*), and C1q and tumor necrosis factor related protein 3 (*C1atnf3*) (Figure 5f). Several functional groups within the 'regulators' were selectively activated under tension. HS showed upregulation of matrix crosslinking enzymes (*Lox*, *Loxl2-3*), procollagen processing proteases (*Adamts4/7/15*, *P4ha1-3*, *Plod2*), matrix-degrading metalloproteases (*Mmp9/11-14/16*), and fibrinolysis inhibitors (*Serpine1/2*, *Serpina3*, *Serpinb6b/b6d/b9*, *Serpinh1*) (Figure 5f). The growth factors *Igf1/2*, *Tgfb3*, and Tgfb ligand *Gdf11* were increased.

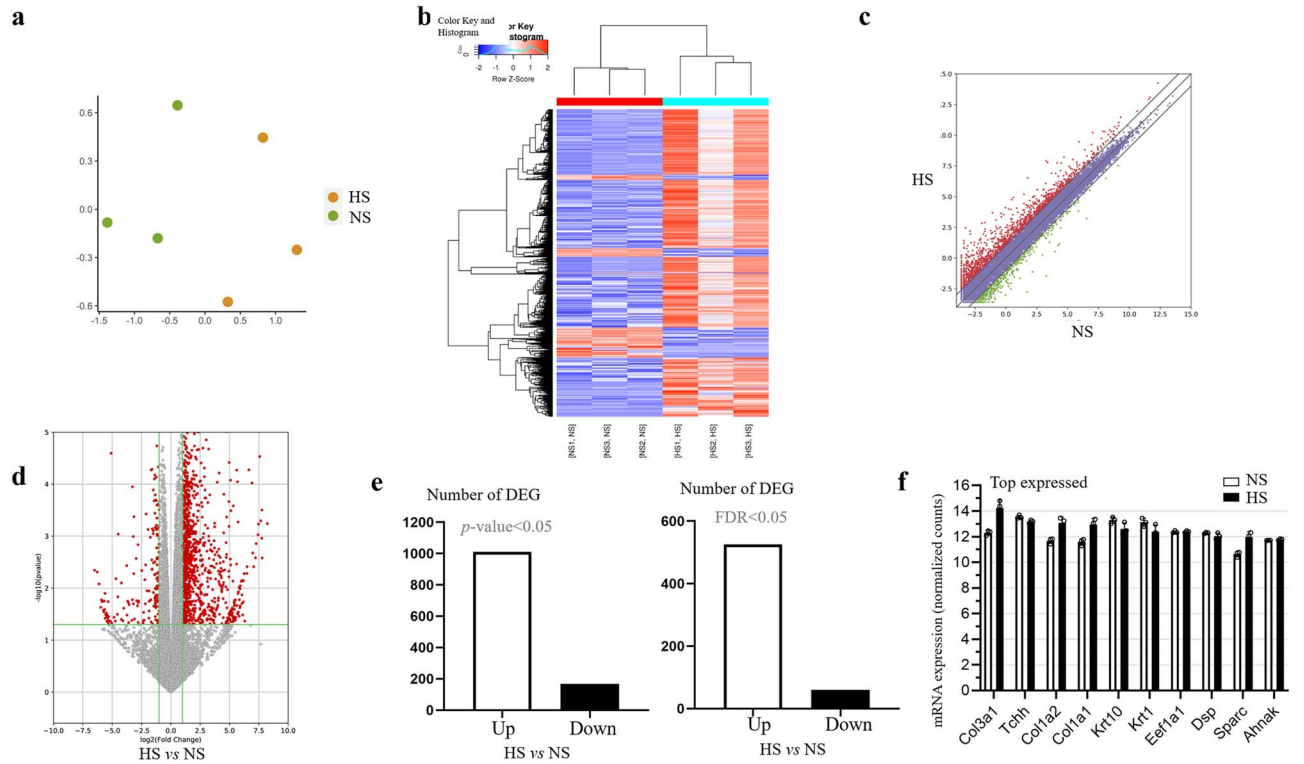


**Figure 4.** Stretching caused a significant change in the transcriptome of HS *vs* NS. (**a**) UMAP analysis of all RNA-sequenced samples from HS and NS groups. (**b**) Heatmap and hierarchical cluster analysis of RNA-sequencing data from HS and NS. (**c**) Scatter plot shows DEGs in HS *vs* NS. (**d**) Volcano plot displays the up- and down-regulated genes in HS *vs* NS. (**e**) Numbers of up- or down-regulated DEGs with *p*-value $< 0.05$ and FDR $< 0.05$. (**f**) Top 10 most expressed genes in HS and their corresponding expression in NS. *HS* hypertrophic scars, *NS* normal scars, *FDR* false discovery rate, *UMAP* uniform manifold approximation and projection, *DEGs* differentially expressed genes

The proangiogenic factors *Angpt2*, *Angptl1*, and *Angptl4* were upregulated. The levels of chemokines, cytokines, and inflammatory mediators were elevated. The Wnt pathway components *Wnt2/2b/9a/16* and the modulator *Sfrp2* were overexpressed. Conversely, the matrix-affiliated genes downregulated in the HS group included the chemokine *Cxcl13* and the bone morphogen *Gdf5* (Figure 5f).

In summary, mRNA sequencing revealed a fibrogenic gene expression profile in suture-anchored scars under tension. HS robustly upregulated the expression of collagenous and non-collagenous ECM components, consistent with increased deposition of disorganized matrix. Growth factors, inflammatory signals, proteases, and crosslinkers that drive aberrant fibrosis were activated. Angiogenic factors and survival pathways were induced. This transcriptomic signature mirrors the histological changes and aligns with human hypertrophic scarring processes.

## Suture-induced hypertrophic scars exhibited transcriptional overlap with mechanically stretched scars

To further validate suture-anchoring as a model of tension-induced scarring, we compared the transcriptional profiles of stretched HS to those of a published model generated using mechanical loading devices (GSE26390) [8]. A total of 41 genes were commonly upregulated between HS and mechanically SS compared to their respective unstretched controls, accounting for 61.2% of the genes upregulated in SS (Figure 6a). Only 3 shared downregulated genes were identified (Figure 6b). GO analysis revealed that the overlapping upregulated genes were enriched in ECM organization, elastic fiber assembly, cellular response to growth factors, and collagen metabolism (Figure 6c, Figure S6, see online supplementary material). The most significant shared cellular component was the collagen-containing matrix, and the shared molecular functions included extracellular structural constituents (Figure 6c, Figure S6, see online supplementary material). Reactome pathway analysis highlighted that ECM organization and collagen fibrillogenesis were conserved between the models (Figure 6d). The collagen genes *Col3a1*, *Col5a2*, *Col8a1*, and *Col12a1* composed the core protein interaction network (Figure 6e). As scarring involves inflammatory signals, we used ImmGen analysis to examine immune associations. The commonly upregulated HS and SS genes were enriched in macrophage and neutrophil signatures (Figure S7a, b, see online supplementary material). The downregulated genes in both cohorts were enriched for innate lymphocytes, macrophages, and neutrophils (Figure S7c, d, see online supplementary material).

These analyses confirmed that suture anchoring elicited highly similar transcriptional changes to those of external mechanical loading, validating the use of tension-induced

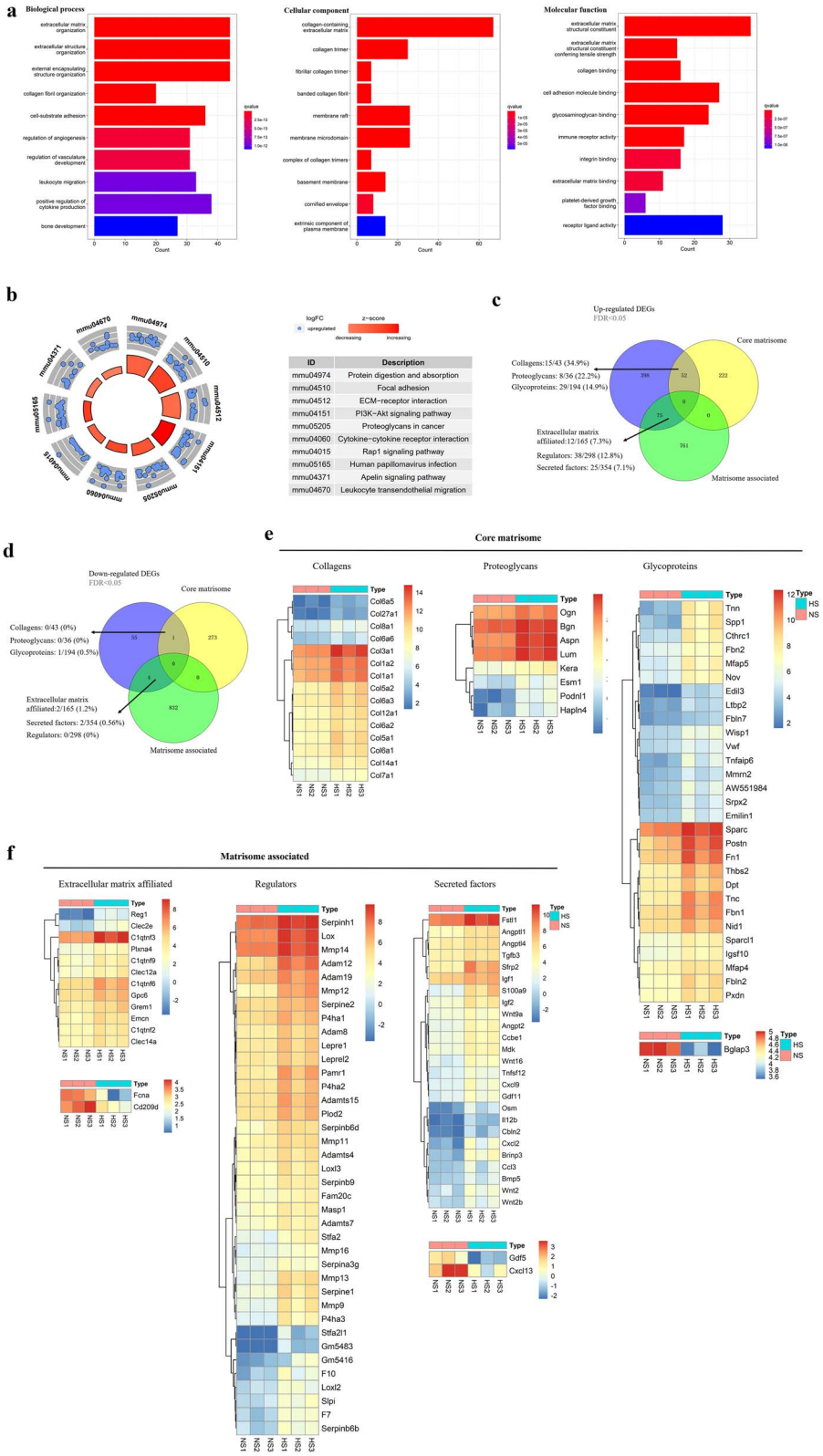


**Figure 5.** Stretching activated ECM-associated pathways and regulated ECM production in scars. (**a**) Bar plot diagrams by GO analysis enriched the upregulated DEGs in biological process, cellular component, and molecular function. (**b**) Cluster circle diagram by KEGG analysis to enrich the upregulated DEGs in HS *vs* NS. Venn diagrams illustrate the proportions of entities within the upregulated (**c**) and downregulated (**d**) DEGs with FDR < 0.05 that were found in the core matrisome and matrisome-associated gene sets. Genes that existed in subcategories are listed with numbers and percentages. DEGs found in subcategories of core matrisome (**e**) and matrisome-associated data sets (**f**) are displayed with heatmap and non-average hierarchical clustered intensity plots. *HS* hypertrophic scars, *NS* normal scars, *ECM* extracellular matrix, *FDR* false discovery rate, *DEG*s differentially expressed genes, *GO* Gene Ontology, *KEGG* Kyoto Encyclopedia of Genes and Genomes

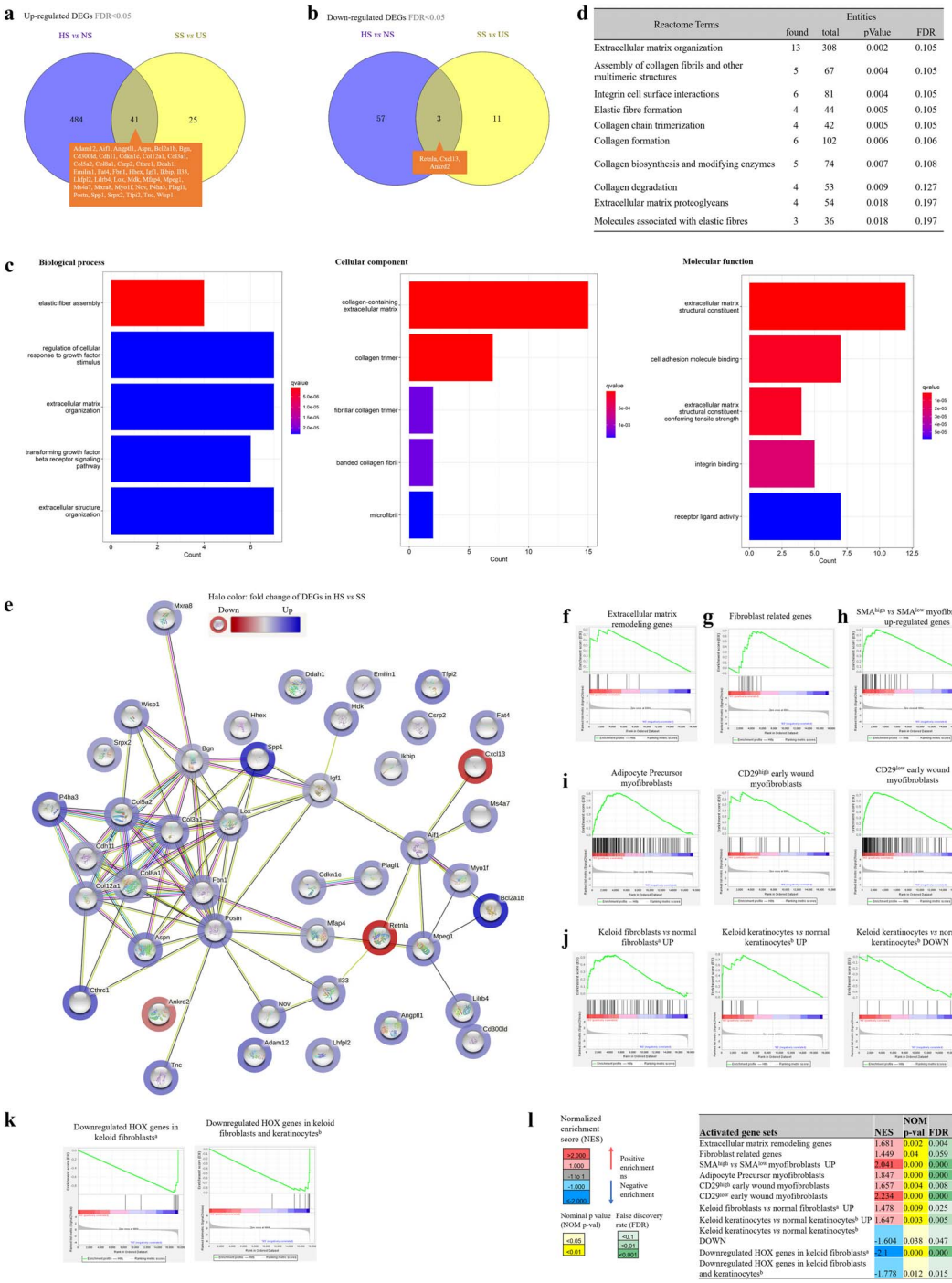


| Reactome Terms | Entities found | total | pValue | FDR |
|---|---|---|---|---|
| Extracellular matrix organization | 13 | 308 | 0.002 | 0.105 |
| Assembly of collagen fibrils and other multimeric structures | 5 | 67 | 0.004 | 0.105 |
| Integrin cell surface interactions | 6 | 81 | 0.004 | 0.105 |
| Elastic fibre formation | 4 | 44 | 0.005 | 0.105 |
| Collagen chain trimerization | 4 | 42 | 0.005 | 0.105 |
| Collagen formation | 6 | 102 | 0.006 | 0.106 |
| Collagen biosynthesis and modifying enzymes | 5 | 74 | 0.007 | 0.108 |
| Collagen degradation | 4 | 53 | 0.009 | 0.127 |
| Extracellular matrix proteoglycans | 4 | 54 | 0.018 | 0.197 |
| Molecules associated with elastic fibres | 3 | 36 | 0.018 | 0.197 |

| Activated gene sets | NES | NOM p-val | FDR |
|---|---|---|---|
| Extracellular matrix remodeling genes | 1.681 | 0.002 | 0.004 |
| Fibroblast related genes | 1.449 | 0.04 | 0.059 |
| SMA$^{high}$ vs SMA$^{low}$ myofibroblasts UP | 2.041 | 0.000 | 0.000 |
| Adipocyte Precursor myofibroblasts | 1.847 | 0.000 | 0.000 |
| CD29$^{high}$ early wound myofibroblasts | 1.657 | 0.004 | 0.008 |
| CD29$^{low}$ early wound myofibroblasts | 2.234 | 0.000 | 0.000 |
| Keloid fibroblasts vs normal fibroblasts[a] UP | 1.478 | 0.009 | 0.025 |
| Keloid keratinocytes vs normal keratinocytes[b] UP | 1.647 | 0.003 | 0.005 |
| Keloid keratinocytes vs normal keratinocytes[b] DOWN | -1.604 | 0.038 | 0.047 |
| Downregulated HOX genes in keloid fibroblasts[a] | 2.1 | 0.000 | 0.000 |
| Downregulated HOX genes in keloid fibroblasts and keratinocytes[b] | -1.778 | 0.012 | 0.015 |

**Figure 6.** Suture stretching-induced scars possessed a transcriptional signature that was similar to mechanical device-induced hypertrophic scars, and stretching created a pro-fibrotic gene expression profile in this model. Venn diagrams depict the common upregulated (**a**) and down-regulated (**b**) DEGs in HS *vs* NS in this model and SS *vs* US using mechanical devices in a reported model. (**c**) GO analysis of the common DEGs in biological process, cellular component, and molecular function. (**d**) Functional enrichment for overlapping transcriptome genes according to Reactome. (**e**) Proteins with values-functional enrichment analysis by STRING analyzed the interaction between shared DEGs with fold-change values in HS *vs* NS. Network nodes represent genes. Halo color represents the fold-change values of DEGs in HS *vs* NS. Edges represent gene–gene associations. (**f–l**) GSEA of gene expression in HS *vs* NS for multiple gene sets collected from ECM, myofibroblasts, fibroblasts, keloid keratinocytes, and fibroblasts. (**f**) Enrichment plot of ECM remodeling gene set. (**g**) Enrichment diagram for fibroblast-related gene set. (**h**) Enrichment graph for upregulated gene set by SMA$^{high}$ myofibroblasts *vs* SMA$^{low}$ myofibroblasts. (**i**) Enrichment plots for adipocyte precursors myofibroblasts, CD29$^{high}$ early wound myofibroblasts, and CD29$^{low}$ early wound myofibroblasts. (**j**) Enrichment diagrams for upregulated gene set in keloid vs. normal fibroblasts, upregulated, and downregulated gene sets in keloid versus normal keratinocytes. (**k**) Enrichment graphs for downregulated HOX gene sets in keloid vs. normal fibroblasts, as well as keloid *vs* normal fibroblasts and keratinocytes. (**l**) Gene signature of HS was subjected to GSEA against activated gene sets from (**f–k**). Normalized enrichment scores (NES), nominal *p* value (NOM *p*-val) and FDR values are shown; NES > 1: positive enrichment (red), NES < −1: negative enrichment (blue); NOM *p*-val and FDR are respectively color coded based on statistical significance (yellow and green). *HS* hypertrophic scars, *NS* normal scars, *ECM* extracellular matrix, *DEGs* differentially expressed genes, *GO* Gene Ontology, *SS* stressed scars, *US* unstressed scars, *STRING* search tool for the retrieval of interacting genes, *HOX* Homeotic, *GSEA* gene-set enrichment analysis

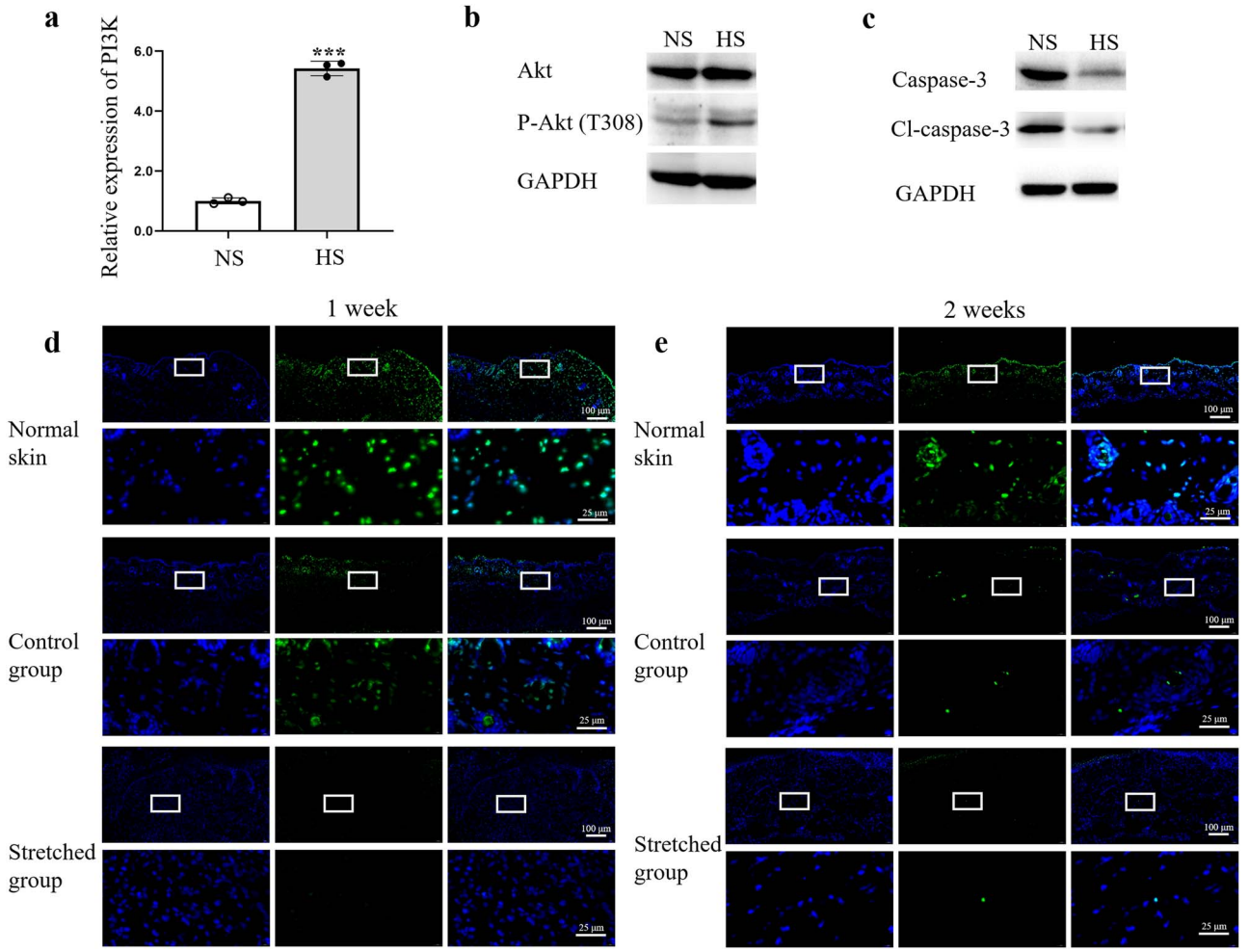


**Figure 7.** PI3K-Akt signaling pathway decreased cellular apoptosis in HS. Scars from HS and NS were harvested at week 2 post-operation. (**a**) Relative expression of PI3K was determined by qRT-PCR. (**b**) Expression of Akt and phosphorylation of Akt was analyzed by WB. (**c**) Expression of caspase-3 and cleaved caspase-3 was measured by WB. (d, e) TUNEL analysis was conducted on scars from HS and NS at weeks 1(**d**) and 2(**e**) post-surgery (Scale bar: 100 $\mu$m & 25 $\mu$m). Values were analyzed by two-tailed Student's t-test. $^{***}P < 0.001$. *HS* hypertrophic scars, *qRT-PCR* Quantitative real-time PCR, *PI3K-Akt* phosphatidylinositol 3-kinase-serine/threonine-protein kinase B, *TUNEL* transferase dUTP nick-end labeling

fibrosis modeling. The shared enrichment of ECM components, collagen pathways, and inflammatory responses demonstrated conserved core mechanisms.

### Suture-induced scars exhibited transcriptional features of myofibroblast activation and keloid pathology

To further validate the fibrotic phenotype, we performed GSEA against published scarring signatures. The expression of genes related to ECM remodeling [38] increased in the 2-week HS group compared with the NS group (Figure 6f). The HS group also exhibited enrichment of a fibroblast-associated gene set [38] (Figure 6g). Compared to the transcriptomic profiles of myofibroblast subpopulations, the HS group was enriched in the upregulated gene set from $SMA^{high}$ myofibroblasts vs. $SMA^{low}$ myofibroblasts [39] (Figure 6h). Specific myofibroblast subsets expanded during wound healing, including adipocyte precursor fibroblasts, $CD29^{high}$ early wound fibroblasts, and $CD29^{low}$ early wound fibroblasts [40]. The HS group showed enrichment of signature genes in all three subsets vs. NS (Figure 6i). To assess keloid-like features, we analyzed HS against cultured human keloid fibroblasts and keratinocytes. The HS group displayed enrichment for both keloid fibroblast[a] [36] and keratinocyte[b] [41] gene sets compared to the NS group (Figure 6j). Mirroring keloid cells, HOX gene sets [36, 41] were negatively enriched in the HS group compared with the NS group (Figure 6k).

In summary, GSEA revealed that the HS group exhibits transcriptional activation of diverse myofibroblast subpopulations and several signatures of human keloid scar cells (Figure 6l). This finding confirmed that localized suture tension elicits key genomic features of fibrotic wound healing.

### Suture tension activated PI3K-Akt signaling to drive fibroproliferation

As transcriptomics predicted increased PI3K-Akt signaling, we examined the activation of this profibrotic pathway in 2-week scars. PI3K mRNA expression and Akt phosphorylation were elevated in HS compared to NS (Figure 7a and b).

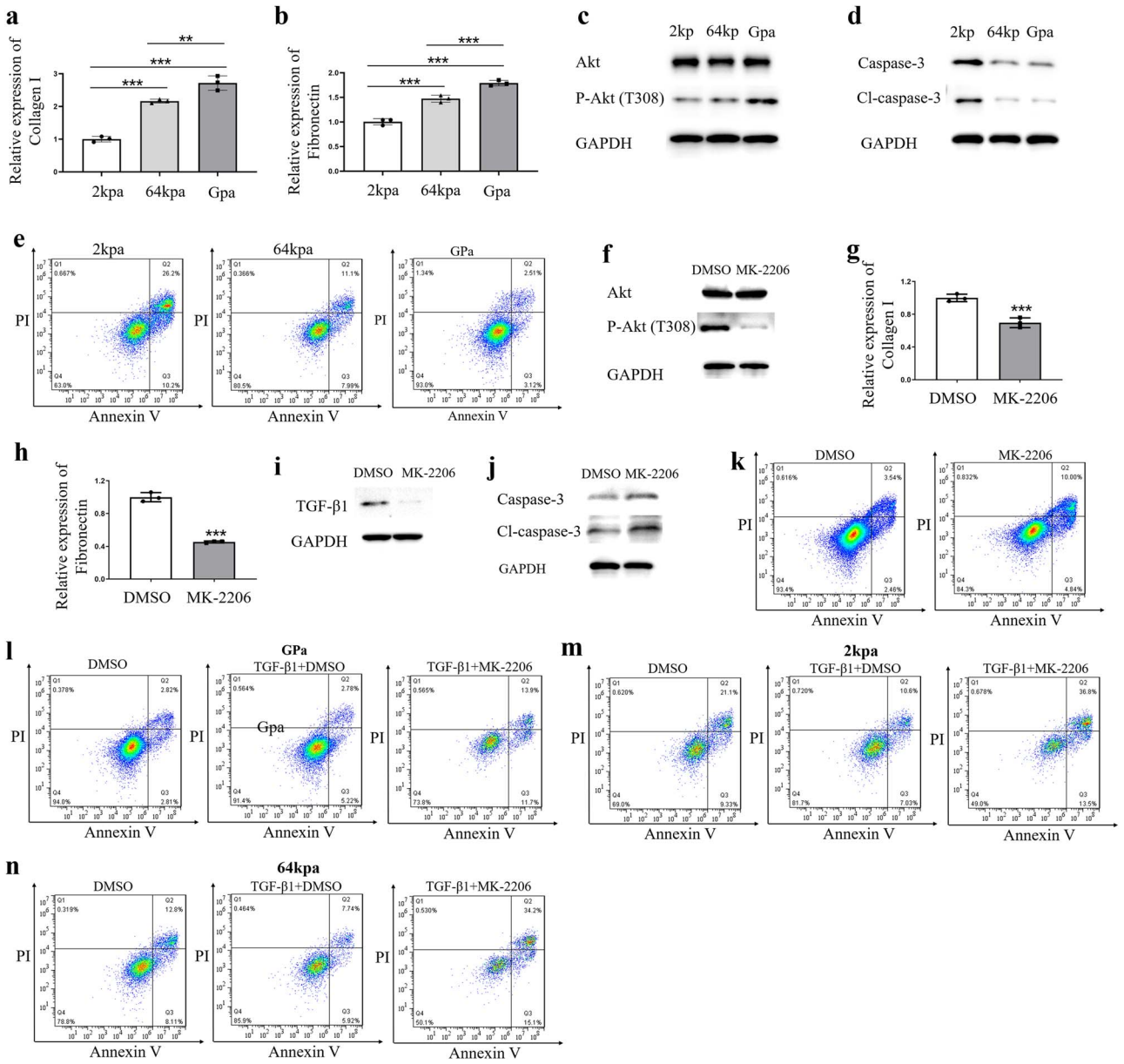


**Figure 8.** Mechanical stretch induced fibrotic gene expression and fibroblast proliferation which can be blocked by MK-2206. Human foreskin fibroblasts-1 (HFF-1) were cultured on silicone substrates (2 and 64 kPa) and stiff plastic substrates (GPa) for 7 days. Relative expression of (**a**) collagen I and (**b**) fibronectin by qRT-PCR. Expression of (**c**) Akt and phosphorylation of Akt by WB, and (**d**) caspase-3 and cleaved caspase-3 by WB. (**e**) HFF-1 cultured on stiff plastic or silicone substrates with 2 or 64 kPa for 48 h. Proportion of early and late stages of apoptotic cell analysis by flow cytometry (FCM). (**f–k**) HFF-1 cultured on stiff plastic were stimulated with MK-2206 (5 $\mu$mol/l) or DMSO for 48 h. (**f**) Expression of Akt and phosphorylation of Akt by WB. Relative expression of (**g**) collagen I and (**h**) fibronectin by qRT-PCR. Expression of (**i**) TGF-$\beta$1 and (**j**) caspase-3 and cleaved caspase-3 by WB. (**k**) Proportion of early and late stages of apoptotic cell analysis by FCM. (**l**) HFF-1 cultivated on stiff plastic were stimulated by TGF-$\beta$1 (100 ng/ml) with MK-2206 (5 $\mu$mol/l) or DMSO for 48 h. Proportion of early and late stages of apoptotic cell analysis by FCM. HFF-1 cultivated on silicone substrates with 2 kPa (**m**) or 64 kPa (**n**) were stimulated by TGF-$\beta$1 (100 ng/ml) with MK-2206 (5 $\mu$mol/l) or DMSO for 48 h. Proportion of early and late stages of apoptotic cell analysis by FCM. Values were analyzed by two-tailed Student's t-test. $^{**}P < 0.05$, $^{***}P < 0.001$. *TGF-$\beta$* transforming growth factor-$\beta$, *qRT-PCR* quantitative real-time PCR

The PI3K-Akt cascade inhibits apoptosis [21, 42]. Accordingly, caspase-3 and cleaved caspase-3 were reduced in the HS group compared with the NS group (Figure 7c). TUNEL immunofluorescence confirmed the decrease in apoptosis in the HS group at weeks 1 and 2 post-wounding (Figure 7d and e). To further explore the effects of PI3K-Akt, we utilized tunable silicone substrates to model matrix stiffening. The normal dermis exhibits an elastic modulus of ~0.1–10 kPa, while fibrotic scars can reach 15–100 kPa [26, 43]. On soft silicone (2 kPa), which mimics normal skin, fibroblasts displayed low fibrosis marker expression (Figure 8a–c). In contrast, on stiff silicone (64 kPa) and plastic (GPa), which resemble fibrotic rigidity, fibroblasts upregulated collagen I, fibronectin, and phosphorylated Akt

(Figure 8a-c). The apoptosis markers caspase-3 and cleaved caspase-3 were decreased on stiff substrates (Figure 8d). Annexin V staining of the cells on stiff vs. soft silicone demonstrated reduced apoptosis (Figure 8e). To test the dependence on Akt signaling, fibroblasts on stiff plastic were treated with the Akt inhibitor MK-2206 [44]. MK-2206 suppressed Akt phosphorylation, collagen I, fibronectin, and TGF-$\beta$1 expression (Figure 8f–i). MK-2206 also increased caspase-3 and cleaved caspase-3 levels and apoptosis (Figure 8j, k). TGF-$\beta$1 treatment reduced apoptosis under all conditions but had a more potent effect on soft 2 kPa silicone, which resembles non-fibrotic skin (Figure 8l–n). The anti-apoptotic effect of TGF-$\beta$1 was abrogated by MK-2206 (Figure 8l–n).

In conclusion, suture tension activated PI3K-Akt signaling in wounds, which was mimicked by matrix stiffening *in vitro*. Akt signaling elicited canonical effects, including fibrosis marker induction, proliferation, and apoptosis resistance. Pharmacologic Akt inhibition reversed fibrosis and restored apoptosis.

## Discussion

In this study, we developed and characterized a novel murine model of hypertrophic scarring induced by localized suture tension. However, due to differences in skin structure, few murine models recapitulate the prolonged wound contraction that leads to granulation tissue formation and pathological scarring clinically [45]. The application of silicone splints around the dorsal wound prevents wound contraction [20]. However, mice are active and silicone splints are easily destroyed or dropped during the experiment, resulting in poor modeling stability. Silicone splints, which are foreign bodies placed near wounds, may also obstruct healing [20]. Aarabi *et al*. generated a linear wound on a murine back [21]. On day 4 post-injury when the wounds were healed, skin stretchers were implanted on both sides of the wounds and mechanical stretcher tension was administered continuously for 10 days [21]. This model was verified to induce hypertrophic scarring resembling human hypertrophic scarring [21]. However, the mechanical load applied to healed wounds does not mimic granulation tissue formation during wound healing and thus cannot precisely simulate scarring processes in humans. Our innovative method used suture anchoring of incisional wounds to impose directional tension throughout the healing process, prolonged wound contraction, generated granulation tissue, and induced scar formation. The suture-anchors frequently burst 2 weeks after surgery and cannot supply tension after the suture breaks but can provide enough tension to prevent wound contraction throughout healing. The scars that formed in this model at week 2 post-surgery were robust histological and molecular hallmarks of mouse mechanical stretched scars and human hypertrophic scars. The modeling period is substantially shorter than that of the rabbit ear and pig models. Hypertrophic scars were conspicuously sustained over 3 months after excision, and mature 6-month scars remained widened and hypercellular with increased fibrotic markers and vasculature, indicating that this model could induce sustained pathological matrix remodeling analogous to human fibroproliferative scarring. Individual differences were controlled by the two wound settings established on each murine upper and lower back. Local suture anchoring avoided repetitive animal restraint or mechanical equipment, which could have caused general confounders. This simple procedure was quite effective, with 90% of the mice developing exuberant scars. Dorsal placement enabled straightforward macroscopic and histologic assessments. Together, these advantages supported this as an accessible and reproducible model of tension-induced hypertrophic scarring.

The results herein implicated PI3K-Akt signaling as a central mediator of sustained fibrosis induced by tension. Transcriptional profiling predicted increased PI3K-Akt activity in stretched scars. *In vitro* experiments validated that mechanical stress induced Akt activity, fibrotic marker expression, and apoptosis resistance, which were all reversed by pharmacologic Akt inhibition. The PI3K-Akt pathway has been shown to participate in pulmonary, renal, and cardiac fibrosis [44, 46, 47]. The PI3K-Akt–mammalian target of rapamycin (mTOR)/6-phosphofructo-2-kinase/fructose-2,6-bisphosphatase 3 (PFKFB3) pathway mediates aerobic glycolysis and collagen synthesis in lung fibroblast in lipopolysaccharide-induced pulmonary fibrosis [48]. Moreover, particulate matter 2.5 activates the PI3K-Akt–mTOR pathway to inhibit autophagy in bronchial epithelial cells and promote epithelial–mesenchymal transition [49]. In cardiac fibrosis, PI3K-Akt regulates angiogenesis after myocardial infarction [47]. In a reported mechanically stretched scar model, the Akt pathway inhibited cellular apoptosis under mechanical forces [21]. As a result, PI3K-Akt represents a critical signaling node during fibrogenesis with potential implications for the development of novel anti-fibrotic strategies. Jiegeng decoction, a traditional Chinese prescription widely used for treating lung diseases, could inhibit apoptosis through the PI3K-Akt signaling pathway by regulating the expression of apoptosis-related proteins, thereby protecting against bleomycin-induced pulmonary fibrosis [50]. MK-2206, a specific Akt signaling inhibitor, effectively reduced TGF-$\beta$1-induced epithelial–mesenchymal transition, fibroblast activation, and ECM deposition and thus improved renal fibrosis [44]. Exosomes derived from human adipose mesenchymal stem cells have been shown to inhibit the PI3K-Akt pathway and thus ameliorate hepatic fibrosis [51]. Besides, it was reported that naringin could inhibit the proliferation and motility of hypertrophic scar fibroblasts, block the cell cycle, and promote apoptosis by reducing Akt kinase activity [42]. Further investigation of the role of the PI3K-Akt pathway in mechanical stress during cutaneous fibrosis will provide therapeutic targets for hypertrophic scars.

Potential limitations should be considered when applying this model. As an acute incisional model, suture-anchored

scars may not adequately reflect all features of cumulative fibrosis in chronic diseases. Moving forward, the model might be adapted to test various interventions by manipulating the timing and direction of imposed tension. Skin defect in the wound margin in this model may enhance hypertrophic scar formation, which can be explored in the future. The murine system enables the exploration of genetic or pharmacologic modulation of factors predicted by transcriptomics and mechanobiology studies. The simplicity and clinical relevance of the suture-anchored tension model will provide a reliable platform for investigating hypertrophic scars.

## Conclusions

Our study established suture-anchored incisions as a novel preclinical model of tension-induced hypertrophic scarring in mice. This facile approach successfully generated cutaneous scars with sustained histological and molecular features resembling human pathological fibrosis. Inhibiting wound contraction was sufficient to activate central drivers of fibroproliferation, such as the PI3K-Akt signaling. The similarities to clinical hypertrophic scarring support this reproducible system as a valuable tool for unraveling mechanisms of matrix overproduction under tension. The results presented here will help guide future research to expand molecular insight and develop targeted anti-scarring therapies.

## Abbreviations

DEG: differentially expressed gene; ECM: Extracellular matrix; FAK: Focal adhesion kinase; FDR: false discovery rate; GO: Gene Ontology; GSEA: Gene set enrichment analysis; H&E: Hematoxylin and eosin; HFF-1: Human foreskin fibroblast; HS: Hypertrophic scars; KEGG: Kyoto Encyclopedia of Genes and Genomes; MRTFA: Myocardin-related transcription factor-A; NES: Normalized enrichment scores; NOM *P*-val: nominal *P* value; NS: Normal scars; PVDF: Polyvinylidenedifluoride; qRT-PCR: Quantitative real-time polymerase chain reaction; SEI: Scar elevation index; $\alpha$-SMA: alpha-Smooth muscle actin; SS: Stressed scars; STRING: Search tool for the retrieval of interacting genes; TGF-$\beta$: Transforming growth factor beta; TUNEL: Terminal deoxynucleotidyl transferase dUTP nick-end labeling; UMAP: Uniform manifold approximation and projection; US: Unstressed scars; VSS: Vancouver scar scale; YAP: Yes-associated protein.

## Author contributions

Yashu Li and Anqi Liu (Conceptualization [equal], Data curation [equal], Formal analysis [equal], Investigation [equal], Methodology [equal], Project administration [equal], Resources [equal], Software [equal], Writing—original draft [equal]), Jingyan Wang (Data curation [supporting], Formal analysis [supporting], Methodology [supporting]), Changsheng Yang (Data curation [supporting], Methodology [supporting], Software [supporting]), Kaiyang Lv (Supervision [equal], Validation [equal], Writing—review & editing [equal]), Weifeng He (Supervision [equal], Validation [equal], Writing—review & editing [equal]), Jun Wu (Supervision [equal], Validation [equal], Writing—review & editing [equal]), and Wenbin Chen (Supervision [lead], Validation [lead], Writing—review & editing [lead].

## Supplementary data

Supplementary data is available at *Burns & Trauma* online.

## Conflict of interest

None declared.

## Funding

This work was supported by the National Natural Science Foundation of China (81772091) and the Clinical Research Plan of Shanghai Hospital Development Center (No. SHDC2020CR3039B).

## Data availability

This published article includes all data generated or analyzed during this study. The RNA-Seq datasets used in this study are available in online NCBI GEO DataSets (GSE243950).

## References

1. Tanaka Y, Miyamoto T, Naito Y, Yoshitake S, Sasahara A, Miyaji K. Randomized study of a new noninvasive skin closure device for use after congenital heart operations. *Ann Thorac Surg* 2016;102:1368–74. https://doi.org/10.1016/j.athoracsur.2016.03.072.
2. Min P, Zhang S, Sinaki DG, Yao P, Hu F, Wang X. *et al.* Using Zhang's supertension-relieving suture technique with slowly-absorbable barbed sutures in the management of pathological scars: a multicenter retrospective study. *Burns Trauma* 2023;11:tkad026. https://doi.org/10.1093/burnst/tkad026.
3. Wang YF, Yang YT, Chen ZA, Wu XL. The running barbed tension-offloading suture: an updated technique update on tension wound closure. *Asian J Surg* 2023;46:3773–6. https://doi.org/10.1016/j.asjsur.2023.05.114.
4. Zhang Q, Shi L, He H, Liu X, Huang Y, Xu D. *et al.* Downregulating scar formation by microneedles directly via a mechanical communication pathway. *ACS Nano* 2022;16:10163–78. https://doi.org/10.1021/acsnano.1c11016.
5. Wang R, Chen B, Wei H, Yan W, Wu Y, Wang C. *et al.* Collecting and deactivating TGF-beta1 hydrogel for anti-scarring therapy in post-glaucoma filtration surgery. *Mater Today Bio* 2022;14:100260. https://doi.org/10.1016/j.mtbio.2022.100260.
6. Wipff PJ, Rifkin DB, Meister JJ, Hinz B. Myofibroblast contraction activates latent TGF-beta1 from the extracellular matrix. *J Cell Biol* 2007;179:1311–23. https://doi.org/10.1083/jcb.200704042.
7. Wong VW, Paterno J, Sorkin M, Glotzbach JP, Levi K, Januszyk M. *et al.* Mechanical force prolongs acute inflammation via T-cell-dependent pathways during scar formation. *FASEB J* 2011;25:4498–510. https://doi.org/10.1096/fj.10-178087.
8. Wong VW, Rustad KC, Akaishi S, Sorkin M, Glotzbach JP, Januszyk M. *et al.* Focal adhesion kinase links mechanical force to skin fibrosis via inflammatory signaling. *Nat Med* 2011;18:148–52. https://doi.org/10.1038/nm.2574.

9. Velasquez LS, Sutherland LB, Liu Z, Grinnell F, Kamm KE, Schneider JW. *et al.* Activation of MRTF-A-dependent gene expression with a small molecule promotes myofibroblast differentiation and wound healing. *Proc Natl Acad Sci USA* 2013;110:16850–5. https://doi.org/10.1073/pnas.1316764110.
10. Francisco J, Zhang Y, Jeong JI, Mizushima W, Ikeda S, Ivessa A. *et al.* Blockade of fibroblast YAP attenuates cardiac fibrosis and dysfunction through MRTF-A inhibition. *JACC Basic Transl Sci* 2020;5:931–45. https://doi.org/10.1016/j.jacbts.2020.07.009.
11. Garoffolo G, Casaburo M, Amadeo F, Salvi M, Bernava G, Piacentini L. *et al.* Reduction of cardiac fibrosis by interference with YAP-dependent transactivation. *Circ Res* 2022;131:239–57. https://doi.org/10.1161/CIRCRESAHA.121.319373.
12. Ragazzini S, Scocozza F, Bernava G, Auricchio F, Colombo GI, Barbuto M. *et al.* Mechanosensor YAP cooperates with TGF-beta1 signaling to promote myofibroblast activation and matrix stiffening in a 3D model of human cardiac fibrosis. *Acta Biomater* 2022;152:300–12.
13. Mascharak S, des Jardins-Park HE, Davitt MF, Griffin M, Borrelli MR, Moore AL. *et al.* Preventing Engrailed-1 activation in fibroblasts yields wound regeneration without scarring. *Science* 2021;372:348–357. https://doi.org/10.1126/science.aba2374.
14. Sun L, Zhang X, Wu S, Liu Y, Guerrero-Juarez CF, Liu W. *et al.* Dynamic interplay between IL-1 and WNT pathways in regulating dermal adipocyte lineage cells during skin development and wound regeneration. *Cell Rep* 2023;42:112647. https://doi.org/10.1016/j.celrep.2023.112647.
15. Kloeters O, Tandara A, Mustoe TA.. Hypertrophic scar model in the rabbit ear: a reproducible model for studying scar tissue behavior with new observations on silicone gel sheeting for scar reduction. *Wound Repair Regen* 2007;15:S40–5. https://doi.org/10.1111/j.1524-475X.2007.00224.x.
16. Momtazi M, Kwan P, Ding J, Anderson CC, Honardoust D, Goekjian S. *et al.* A nude mouse model of hypertrophic scar shows morphologic and histologic characteristics of human hypertrophic scar. *Wound Repair Regen* 2013;21:77–87. https://doi.org/10.1111/j.1524-475X.2012.00856.x.
17. Li J, Ng SK, Xi W, Zhang Z, Wang X, Li H. *et al.* Efficacy and safety of a dual-scan protocol for carbon dioxide laser in the treatment of split-thickness skin graft contraction in a red Duroc pig model. *Burns Trauma* 2021;9:tkab048. https://doi.org/10.1093/burnst/tkab048.
18. Chen JS, Longaker MT, Gurtner GC.. Murine models of human wound healing. *Methods Mol Biol* 2013;1037:265–74. https://doi.org/10.1007/978-1-62703-505-7_15.
19. Wong VW, Sorkin M, Glotzbach JP, Longaker MT, Gurtner GC. Surgical approaches to create murine models of human wound healing. *J Biomed Biotechnol* 2011;2011:969618. https://doi.org/10.1155/2011/969618.
20. Wang X, Ge J, Tredget EE, Wu Y. The mouse excisional wound splinting model, including applications for stem cell transplantation. *Nat Protoc* 2013;8:302–9. https://doi.org/10.1038/nprot.2013.002.
21. Aarabi S, Bhatt KA, Shi Y, Paterno J, Chang EI, Loh SA. *et al.* Mechanical load initiates hypertrophic scar formation through decreased cellular apoptosis. *FASEB J* 2007;21:3250–61. https://doi.org/10.1096/fj.07-8218com.
22. Claytor RB, Sheck CG, Chopra V.. Microneedling outcomes in early postsurgical scars. *Plast Reconstr Surg* 2022;150:557e–61. https://doi.org/10.1097/PRS.0000000000009466.
23. Zhou S, Wang W, Zhou S, Zhang G, He J, Li Q. A novel model for cutaneous wound healing and scarring in the rat. *Plast Reconstr Surg* 2019;143:468–77. https://doi.org/10.1097/PRS.0000000000005274.
24. Wietecha MS, Pensalfini M, Cangkrama M, Muller B, Jin J, Brinckmann J. *et al.* Activin-mediated alterations of the fibroblast transcriptome and matrisome control the biomechanical properties of skin wounds. *Nat Commun* 2020;11:2604.
25. Li Y, Wang J, Wang Y, He W, Zhang Y, Liu Y. IL-1beta/NF-kappaB signaling inhibits IGF-1 production via let-7f-5p in dendritic epidermal T cells. *J Leukoc Biol* 2022;112:1677–90. https://doi.org/10.1002/JLB.3MA0322-171R.
26. Achterberg VF, Buscemi L, Diekmann H, Smith-Clerc J, Schwengler H, Meister JJ. *et al.* The nano-scale mechanical properties of the extracellular matrix regulate dermal fibroblast function. *J Invest Dermatol* 2014;134:1862–72. https://doi.org/10.1038/jid.2014.90.
27. George N, Fexova S, Fuentes AM, Madrigal P, Bi Y, Iqbal H. *et al.* Expression atlas update: insights from sequencing data at both bulk and single cell level. *Nucleic Acids Res* 2023;52:D107–14. https://doi.org/10.1093/nar/gkad1021.
28. Ye C, Zhu J, Wang J, Chen D, Meng L, Zhan Y. *et al.* Single-cell and spatial transcriptomics reveal the fibrosis-related immune landscape of biliary atresia. *Clin Transl Med* 2022;12:e1070. https://doi.org/10.1002/ctm2.1070.
29. Naba A, Clauser KR, Ding H, Whittaker CA, Carr SA, Hynes RO. The extracellular matrix: tools and insights for the "omics" era. *Matrix Biol* 2016;49:10–24. https://doi.org/10.1016/j.matbio.2015.06.003.
30. Shay T, Kang J. Immunological genome project and systems immunology. *Trends Immunol* 2013;34:602–9. https://doi.org/10.1016/j.it.2013.03.004.
31. Zhao S, Liu H, Wang H, He X, Tang J, Qi S. *et al.* Inhibition of phosphatidylinositol 3-kinase catalytic subunit alpha by miR-203a-3p reduces hypertrophic scar formation via phosphatidylinositol 3-kinase/AKT/mTOR signaling pathway. *Burns Trauma* 2024;12:tkad048. https://doi.org/10.1093/burnst/tkad048.
32. Kwansa AL, De Vita R, Freeman JW.. Mechanical recruitment of N- and C-crosslinks in collagen type I. *Matrix Biol* 2014;34:161–9. https://doi.org/10.1016/j.matbio.2013.10.012.
33. Wang ZC, Zhao WY, Cao Y, Liu YQ, Sun Q, Shi P. *et al.* The roles of inflammation in keloid and hypertrophic scars. *Front Immunol* 2020;11:603187. https://doi.org/10.3389/fimmu.2020.603187.
34. Limandjaja GC, Belien JM, Scheper RJ, Niessen FB, Gibbs S. Hypertrophic and keloid scars fail to progress from the CD34(−) /alpha-smooth muscle actin (alpha-SMA)(+) immature scar phenotype and show gradient differences in alpha-SMA and p16 expression. *Br J Dermatol* 2020;182:974–86. https://doi.org/10.1111/bjd.18219.
35. Cheng L, Sun X, Zhao X, Wang L, Yu J, Pan G. *et al.* Surface biofunctional drug-loaded electrospun fibrous scaffolds for comprehensive repairing hypertrophic scars. *Biomaterials* 2016;83:169–81. https://doi.org/10.1016/j.biomaterials.2016.01.002.
36. Smith JC, Boone BE, Opalenik SR, Williams SM, Russell SB. Gene profiling of keloid fibroblasts shows altered expression in multiple fibrosis-associated pathways. *J Invest Dermatol* 2008;128:1298–310. https://doi.org/10.1038/sj.jid.5701149.

37. Agrawal A, Ding J, Agrawal B, Kwan PO, Tredget EE. Stimulation of toll-like receptor pathways by burn eschar tissue as a possible mechanism for hypertrophic scarring. *Wound Repair Regen* 2021;29:810–9. https://doi.org/10.1111/wrr.12940.
38. Rinkevich Y, Walmsley GG, Hu MS, Maan ZN, Newman AM, Drukker M. *et al.* Skin fibrosis. Identification and isolation of a dermal lineage with intrinsic fibrogenic potential. *Science* 2015;348:aaa2151.
39. Bergmeier V, Etich J, Pitzler L, Frie C, Koch M, Fischer M. *et al.* Identification of a myofibroblast-specific expression signature in skin wounds. *Matrix Biol* 2018;65:59–74. https://doi.org/10.1016/j.matbio.2017.07.005.
40. Shook BA, Wasko RR, Rivera-Gonzalez GC, Salazar-Gatzimas E, Lopez-Giraldez F, Dash BC. *et al.* Myofibroblast proliferation and heterogeneity are supported by macrophages during skin repair. *Science* 2018;362:891–899. https://doi.org/10.1126/science.aar2971.
41. Hahn JM, Glaser K, McFarland KL, Aronow BJ, Boyce ST, Supp DM. Keloid-derived keratinocytes exhibit an abnormal gene expression profile consistent with a distinct causal role in keloid pathology. *Wound Repair Regen* 2013;21:530–44. https://doi.org/10.1111/wrr.12060.
42. Song Y, Guo B, Ma S, Chang P, Tao K. Naringin suppresses the growth and motility of hypertrophic scar fibroblasts by inhibiting the kinase activity of Akt. *Biomed Pharmacother* 2018;105:1291–8. https://doi.org/10.1016/j.biopha.2018.06.103.
43. Wang Y, Liu M, Zhang W, Liu H,Jin F, Mao S. *et al.* Mechanical strategies to promote vascularization for tissue engineering and regenerative medicine. *Burns Trauma* 2024;12:tkae039. https://doi.org/10.1093/burnst/tkae039.
44. Chen M, Yu Y, Mi T, Guo Q, Xiang B, Tian X. *et al.* MK-2206 alleviates renal fibrosis by suppressing the Akt/mTOR Signaling pathway In vivo and In vitro. *Cells* 2022;11. https://doi.org/10.3390/cells11213505.
45. Li J, Wang J, Wang Z, Xia Y, Zhou M, Zhong A. *et al.* Experimental models for cutaneous hypertrophic scar research. *Wound Repair Regen* 2020;28:126–44. https://doi.org/10.1111/wrr.12760.
46. Wang J, Hu K, Cai X, Yang B, He Q, Wang J. *et al.* Targeting PI3K/AKT signaling for treatment of idiopathic pulmonary fibrosis. *Acta Pharm Sin B* 2022;12:18–32. https://doi.org/10.1016/j.apsb.2021.07.023.
47. Zhang Q, Wang L, Wang S, Cheng H, Xu L, Pei G. *et al.* Signaling pathways and targeted therapy for myocardial infarction. *Signal Transduct Target Ther* 2022;7:78.
48. Hu X, Xu Q, Wan H, Hu Y, Xing S, Yang H. *et al.* PI3K-Akt-mTOR/PFKFB3 pathway mediated lung fibroblast aerobic glycolysis and collagen synthesis in lipopolysaccharide-induced pulmonary fibrosis. *Lab Investig* 2020;100:801–11. https://doi.org/10.1038/s41374-020-0404-9.
49. Cong LH, Li T, Wang H, Wu YN, Wang SP, Zhao YY. *et al.* IL-17A-producing T cells exacerbate fine particulate matter-induced lung inflammation and fibrosis by inhibiting PI3K/Akt/mTOR-mediated autophagy. *J Cell Mol Med* 2020;24:8532–44. https://doi.org/10.1111/jcmm.15475.
50. Xu Y, Wang X, Han D, Wang J, Luo Z, Jin T. *et al.* Revealing the mechanism of Jiegeng decoction attenuates bleomycin-induced pulmonary fibrosis via PI3K/Akt signaling pathway based on lipidomics and transcriptomics. *Phytomedicine* 2022;102:154207. https://doi.org/10.1016/j.phymed.2022.154207.
51. Zhang Z, Shang J, Yang Q, Dai Z, Liang Y, Lai C. *et al.* Exosomes derived from human adipose mesenchymal stem cells ameliorate hepatic fibrosis by inhibiting PI3K/Akt/mTOR pathway and remodeling choline metabolism. *J Nanobiotechnology* 2023;21:29.